

ORIGINAL ARTICLE

An Improved Aerodynamic Model for Quasi-Steady Simulations of Animal Flight at Moderate Reynolds Numbers

Yunxing Su^{1,2} | Xiaozhou Fan^{1,3}  | Kyohei Onoue^{1,4} | Hamid Vejdani^{1,5} | Kenneth S. Breuer¹

¹Center for Fluid Mechanics, School of Engineering, Brown University, Providence, Rhode Island, USA | ²Mechanical and Industrial Engineering Department, University of Minnesota, Duluth, Minnesota, USA | ³Sustainable Energy and Environment, The Hong Kong University of Science and Technology, Guangzhou, China | ⁴Honda Aircraft Company, Greensboro, North Carolina, USA | ⁵Mechanical Engineering Department, Lawrence Technological University, Southfield, Michigan, USA

Correspondence: Xiaozhou Fan (xiaozhoufan@hkust-gz.edu.cn)

Received: 13 March 2025 | **Revised:** 30 August 2025 | **Accepted:** 18 September 2025

Keywords: animal locomotion | experimental fluid mechanics | reduced-order modeling | vortex dynamics

ABSTRACT

We present experimental and numerical studies aimed at improving models of animal flight at moderate Reynolds numbers ($20k-50k$). Quasi-steady aerodynamic force and moment data were collected using a rectangular wing across various angles of attack, α . The drag coefficient, $C_D(\alpha)$, is well described by a simple trigonometric function, while the lift coefficient, $C_L(\alpha)$, combines trigonometric and exponential terms—the latter capturing the linear behavior at small α predicted by inviscid theory. We also derive an empirical relation for the center of pressure as a function of α , allowing evaluation of the pitching moment coefficient, $C_M(\alpha)$, about any axis. These formulas are integrated into a dynamic flapping wing model to simulate forward flight of a pigeon and a bat at different speeds. Compared to prior models, our approach yields better agreement with wingbeat frequency data, particularly at high speeds. The small α angle regime proves especially beneficial, offering higher C_L/C_D , which translates to reduced power demands and smaller body pitch variation—key considerations for the design of flapping wing robots.

1 | Introduction

There has been a substantial interest in understanding the physics behind flapping flight in birds and bats, both to understand the intricate mechanics of these natural fliers and to pave the way for the development of micro air vehicles (MAVs) that mirror their counterparts, offering superior maneuverability, efficiency, and payload capabilities [1, 2]. Significant advancement has been made in understanding the aerodynamics of flapping flight [3–9]. The existing research is predominantly focused on relatively small fliers such as insects, characterized by Reynolds numbers less than 1000 [10–14]. However, when examining larger fliers like

birds and bats, the Reynolds number substantially increases to approximately 40,000 [15–18]. Given that a significant proportion of contemporary MAVs operate within this intermediate range of Reynolds numbers, a computationally efficient aerodynamic model that connects the wing aerodynamic forces to the angle of attack, α , is required for designing controllers and studying the stability for these vehicles.

Various aerodynamic models with distinct characteristics are employed in the examination of animal flight. For example, the quasi-steady techniques proposed in the literature [11–13] have been extensively used for modeling aerodynamic forces [19–22],

Yunxing Su and Xiaozhou Fan contributed equally to this work. Xiaozhou Fan conducted the work when he was at Caltech GALCIT.

due to their simple nature and low computational cost, making it highly practical for tasks such as dynamical modeling, control, and optimization calculations. Cheng et al. [21] employ this quasi-steady modeling together with blade element theory to analyze the flight mechanics and control of escaping maneuvers in hummingbirds. The authors applied a framework to model translational lift and drag similar to Dickinson et al. [11], but adjusted slightly the numerical values of the aerodynamic model specifically for hummingbirds with insights from computational fluid dynamics (CFD) simulations [23]. Berman and Wang [14] used blade element theory together with the quasi-steady model [11, 13] to calculate the aerodynamic forces for their modeling of hawkmoth and fruitfly. Using this model, the authors [14] successfully identified the most efficient wing movements of hovering insect flight that minimize power consumption while ensuring sufficient lift to maintain a consistent average altitude throughout a single flapping period.

However, the simple sinusoidal aerodynamic force coefficients used in this model [11] might not be applicable at the moderate to high Reynolds number range of 10^4 – 10^5 , typical for larger birds or bats at cruise speed. Ellington [24] reported that the high force coefficients observed in the flapping wings of insects [11, 25–27] may not persist at Reynolds numbers relevant for bird flight (hummingbird may be an aerodynamic transitional regime between insects and birds). Consequently, numerous researchers have customized and refined this model to better align with their specific requirements and enhance its accuracy. In particular, Parslew [19] used blade element theory to capture the high-lift-to-drag ratios experienced at low angles of attack (-18° to 14°) and successfully captured the pigeon cruise flight mode. Based on their aerodynamic model, Parslew and Crowther [20] and Parslew [19] successfully developed a predictive model to analyze pigeon flight for different flight modes (cruise, climbing, and descending) over a range of forward speeds.

The Dickinson and Sane model was developed based on the experiments mimicking the aerodynamic performance of insect flight at a Reynolds number of the order of 100. However, Dickinson and Götz [10] show that the aerodynamic performance of translating wings is highly sensitive to the Reynolds number. At high Reynolds number, linear inviscid theory predicts that the slope of $C_L - \alpha$ should be 2π for small angle of α below the stall angle [28]. In contrast, Dickinson et al. [11] measured a much lower value around 3.8. When used at larger Reynolds number, the drag model $C_D - \alpha$ measured at low Reynolds number also tends to be larger than true values, which may explain the lower-than-observed thrust predicted for cruising bat flight [18]. Similar direct applications of the low Re formulation to high Reynolds number cases may also be found in the literature [19–21, 29–32].

Of course, researchers have also utilized approaches different from quasi-steady modeling to understand $C_L, C_D - \alpha$ at $Re \sim 10^4$ – 10^5 . Carruthers et al. [33, 34] performed steady panel method computations with wing profiles reconstructed from still images of flapping bird wings, and demonstrated that birds utilize not only wing morphing but also tails to rapidly transit to perching. Usherwood [35] investigated the aerodynamic performance of a revolving, dried pigeon wing and a flat plate replica using both direct force transducer and pressure sensor measurements at Reynolds number up to 10,800. For both cases (dried pigeon

wing and flat plate), high lift coefficients are obtained with the maximum lift force achieved at an angle of attack up to 43° . In addition, Taha et al. [36] utilized a state-space representation of the unsteady aerodynamics of flapping flight and proposed a reduced-order model for flight dynamics and control. The model extends Duhamel's principle to unconventional lift curves, aiming specifically to incorporate the contribution of the leading-edge vortex (LEV).

Nevertheless, quasi-steady modeling retains considerable appeal for its simplicity and accuracy, and thus, in this study, we propose improvements to the Sane–Dickinson quasi-steady formulation for lift and drag that are relevant at the moderate to large Reynolds numbers pertinent to avian and bat flight. In addition, it has been proven challenging to accurately predict the pitching motion of a flapping wing flight robot or animals [17, 37] due to the lack of reliable data on the change of wing center of pressure with α (see exception for low Reynolds number [38]). To address this concern, we also present pitching moment measurements over this moderate to high Reynolds number range.

2 | Materials and Methods

2.1 | Experimental Setup

All experiments were conducted in a closed-return water channel with a test section of 0.8 m in width and 0.6 m in depth. Figure 1A illustrates a flat plate with a chord, $c = 0.076$ m, span, $h = 0.456$ m, and thickness, $\delta = 8$ mm, rigidly affixed to the 6-axis force transducer (Delta IP65, ATI Industrial Automation), in a uniform free-stream with velocity, U , and density, ρ_f . An end plate is installed to eliminate the spanwise flow, which promotes the 2D nature of the experiment. The free-stream velocity was monitored in real time using an acoustic Doppler velocimeter (Vectrino, Nortek AS). The force transducer measures the normal, F_N , and tangential, F_T , forces, as well as the pitching moment, M , about the rotational axis located at the mid-chord point. These forces are related to lift, L , and drag, D , forces through the geometry shown in Figure 1B,

$$\begin{aligned} L &= F_N \cos(\alpha) - F_T \sin(\alpha), \\ D &= F_N \sin(\alpha) + F_T \cos(\alpha), \end{aligned} \quad (1)$$

where α denotes the geometric angle of attack. The angle of attack is modulated by sending an open-loop command to the rotary stepper motor (Nema23 D600, Applied Motion Products), and the corresponding value is measured via an optical encoder (E3 optical encoder, US Digital). More details about the experimental setup can be found in our previous work [39–41]. In this study, the Reynolds number, based on the chord length, is defined as $Re = Uc/\nu$, where ν denotes the kinematic viscosity of the fluid. Given that the chord length represents less than 10% of the test section width, the blockage and side-wall boundary layer effects were deemed minor. Due to the use of a large aspect ratio ($AR = 6$) rectangular plate, the flow associated with the present study is expected to be largely two-dimensional, and the validity of this assumption will be justified in a subsequent section.

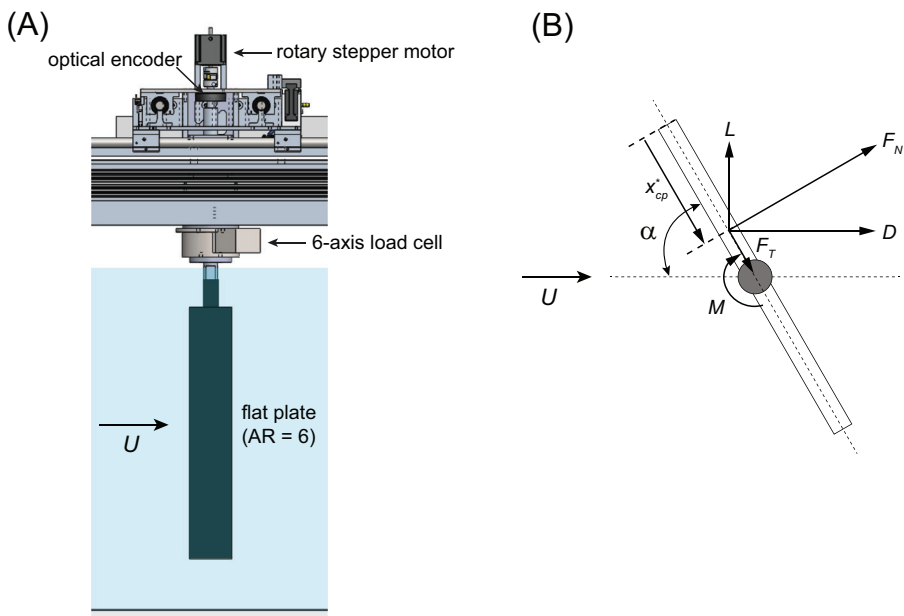


FIGURE 1 | The experimental setup. (A) Schematic of the experimental set-up, illustrating a flat plate ($AR = 6$) mounted on a 6-axis load cell about its mid-chord location. The flat plate is immersed in a uniform flow with a free-stream velocity, U . The present setup allows for a direct measurement of normal and tangential forces, as well as the pitching moment exerted on a flat plate. The angle of attack, α , is accurately measured and modulated via the optical encoder and the rotary stepper motor using an open-loop command. (B) Definition of the forces and moment imparted on a flat plate, which is subject to freestream U , with angle of attack α . Lift (L) and drag (D) are approximated by decomposing the forces (F_N and F_T) into components along the streamwise and transverse directions. The normalized center of pressure, x_{cp}^* , is measured from the leading edge.

In the present investigation, the steady-state forces and moment associated with a steady flat plate immersed in a uniform flow were measured over a broad range of angles of attack ($\alpha = 0^\circ \sim 110^\circ$, $\Delta\alpha = 2^\circ$) at four different Reynolds numbers varying from 20,000 to 50,000 at an increment of 10,000. At each angle of attack, the measurements were recorded for 30 s, but only the last 20 s of the recording was analyzed during the post-processing in order to exclude any transient response. The reproducibility of the results was confirmed by repeating the same set of experiments three times.

Another useful contribution of the present study is the establishment of a simple empirical relation between the location of the center of pressure and the angle of attack. We determined the chordwise location of the center of pressure, x_{cp}^* (measured from the leading edge), using the formula:

$$x_{cp}^* = 0.5 - M/(F_N c), \quad (2)$$

where M is measured pitching moment, F_N is measured normal force, and c is chord length.

2.2 | Simulation of Flapping Flight Using Proposed Model

The modeling of the flapping wing dynamical system is detailed in related papers [16, 42], but is also summarized here for completeness.

In a nutshell, we use the quasi-steady blade element approach to model aerodynamic forces, and apply optimization on the flight

trajectory of a wing-body dynamical system with a prescribed flight speed. More specifically, the motions we consider are parameterized by flapping frequency, flapping amplitude, and pitching amplitude. A numerical optimization is used to find wing kinematics, with lowest flapping frequency possible, that yield a stable periodic solution for a prescribed flight speed.

Two distinct flapping wing animals—a rock pigeon and a yellow-bellied sheath-tailed bat—are modeled to showcase the proposed quasi-steady aerodynamic models from low to high Re regime. The morphology of the pigeon model is adapted from Tobalske and Dial [43], with the whole mass $M = 0.316$ kg, length of each wing $b/2 = 27.9$ cm, and average wing chord $c = 11.2$ cm. The morphology of the bat model is taken from the measurements of Norberg and Åke Norberg [44], with mass $M = 0.068$ kg, length of each wing $b/2 = 30$ cm, and average wing chord $c = 10$ cm. Since the focus of this paper is to compare the effectiveness of the proposed high aerodynamic model Re , we abstracted the wings of pigeons and bats into rectangles, as the shape of the wing does not have a significant impact on the optimization results according to our previous study [16].

In the global inertial coordinate, \mathbf{G} , the animal body has two translational degrees of freedom (DoF) ($x - z$) and one rotational degree of freedom in pitch (θ_b), where the latter accounts for the changes in the body angle, as illustrated in Figure 2A. We denote the body kinematics as $\mathbf{q}_b = [x, z, \theta_b]^T$. The model allows modulation of its wingspan during the wingbeat cycle in order to replicate basic wing kinematics of a pigeon [16]. For the simulation of highly articulated bat wing (Figure 2B), we incorporate a small amount of wing folding, and a linearly varying pitching angles from root to tip (wing twisting) [42].

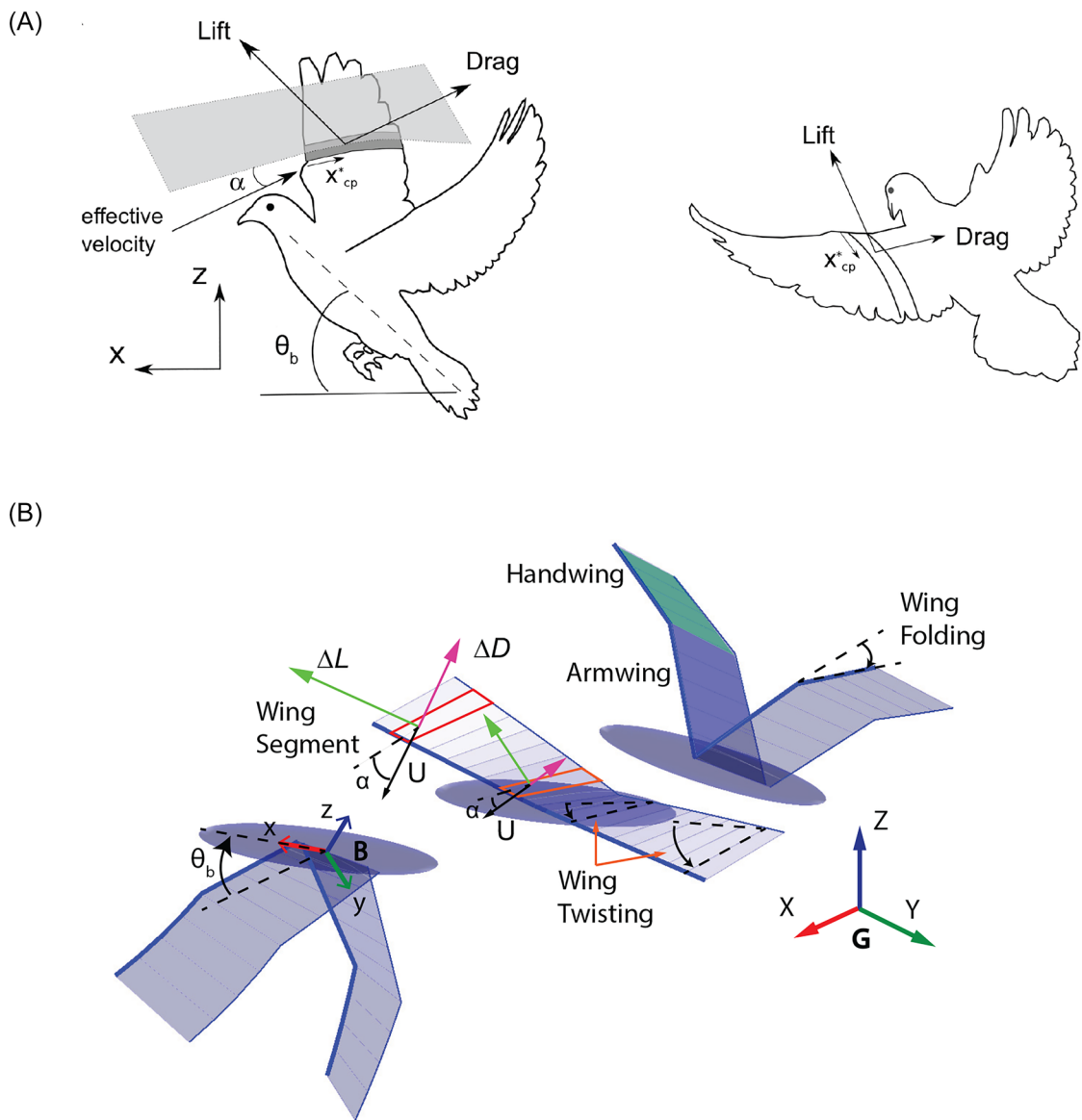


FIGURE 2 | Schematic of the simulation. (A) Model with two translational degrees of freedom ($x - z$) and one rotational degree of freedom in pitch for the body angle (ψ). In addition to producing flapping and pronation/supination motions, the pigeon wings feature spanwise inward and outward retraction. (B) Flight trajectories of simulated flapping wing-body system, with a simplified cigar-shape body and two rectangular-shaped wings. The simulation of highly articulated batwing has a small wing folding (additional rotation of handwing against armwing) and wing twisting (linear variation of pitch angle). Two wing segments (one inboard and one outboard) are outlined along with their effective velocities, U , and angles of attack, α . The ensuing segment-wise lift, ΔL (green arrows), and drag, ΔD (magenta arrows), are also presented.

More specifically, the wing folding refers to additional rotation of outboard handwing with respect to inboard armwing (Figure 2B), and is sinusoidal in time, with folding angle at mid-downstroke being zero, and mid-upstroke being maximum folding angle of 10°. The wing twisting means that the ratio of pitch angles between the wing tip and wing root is ξ —and is fixed to be 1.6 for all simulations. Note, these two wing kinematics are considered to be parameters and their values will not change during the optimization process.

Blade element theory [18, 20, 45] is used to model the aerodynamic forces. Specifically, the left and right wings are divided into $N = 10$ equal width segments (Figure 2B), with each segment approximating a 2D airfoil in quasi-steady state, which generates

a local lift and drag force vector. The total force is then a vector summation over the elemental forces on each segment in the global coordinate, \mathbf{G} . It is worth mentioning that the angle of attack, α , seen by each wing segment is different due to the different velocities of each wing segment. Specifically, the segment-wise lift, ΔL , and drag, ΔD , forces are then given as

$$\Delta L = 1/2\rho C_L U_G^2 c \Delta r, \quad (3)$$

$$\Delta D = 1/2\rho C_D U_G^2 c \Delta r, \quad (4)$$

where ρ , c , Δr , and U_G are the air density, chord length, segment width, and airspeed at each segment in the global coordinate system, \mathbf{G} . The lift and drag on each segment are located at the quarter-chord; in other words, in the simulation, we ignored the change of center of pressure x_{cp} as a function of angle of attack α . Note, the aerodynamic coefficients (C_L and C_D) used in the lift and drag model are taken from Dickinson et al. [11] and current study, respectively. Each segment-wise force will impart a torque on the body, and the total torques felt by the body are the summation of all wing segments, assuming left and right symmetry. Note that the tail is not modeled in the current formulation, and that the massed body has a moment of inertia, but is, otherwise, aerodynamically passive.

To construct the equations of motion, we assume the left and right wing motions to be symmetric. Thus, the dynamical model has 5 DoF in total: the animal position, x, z , body pitch angle θ_b , and the wing root flapping and pitching amplitudes, ϕ_r and θ_r , respectively.

Along with their derivatives, they form a 10 by 1 state vector \mathbf{q} with which we construct the Lagrangian equation of motion:

$$\mathbf{D}(\mathbf{q})\ddot{\mathbf{q}} + \mathbf{C}(\mathbf{q}, \dot{\mathbf{q}})\dot{\mathbf{q}} + \mathbf{g}(\mathbf{q}) = \boldsymbol{\tau} + \mathbf{f}_{aero}, \quad (5)$$

where \mathbf{D} , $\mathbf{C}(\mathbf{q}, \dot{\mathbf{q}})$, and $\mathbf{g}(\mathbf{q})$ are the mass matrix, centrifugal matrix, and gravitational vector, respectively. The generalized torque, $\boldsymbol{\tau} = [0_{1 \times 3}, \tau_w]^T$, denotes the internal forces between the wing and the body, while \mathbf{f}_{aero} represents the external aerodynamic forces and the ensuing torques felt by both left and right wings.

Mathematically, steady forward flight is a solution to the equations of motion that satisfy

$$[\mathbf{q}, \dot{\mathbf{q}}]_t = [\mathbf{q}, \dot{\mathbf{q}}]_{t+T} + \Delta \cdot T, \quad (6)$$

where t is an arbitrary instant of time, T is wingbeat period (also being the objective function). Δ is a 10-valued vector, $\Delta = [U_x, U_z, 0, 0, 0, 0, 0, 0, 0, 0]^T$. Here, U_x and U_z are the cycle-averaged velocity components along the forward (X) and vertical (Z) directions in the global coordinate system, \mathbf{G} , and are defined as inputs. If $U_x, U_z = 0$, this becomes the more familiar expression for hovering flight.

In this paper, we focus on forward and level flight ($U_z = 0$). As pointed out earlier, there are many sets of possible wing kinematic parameters that may satisfy the constraints (Equation 6), given appropriate initial conditions $(\mathbf{q}_0, \dot{\mathbf{q}}_0)$. Therefore, an optimization scheme is employed that searches over all (realistic) candidates of wing kinematics that result in the prescribed forward speed, U_x , and finds the one with minimum frequency, f . Concretely, we integrate the coupled wings and body dynamical system from initial guess \mathbf{q}_0 over one wingbeat cycle T , and used shooting method in conjunction with the Newton–Raphson technique to find wing kinematics that would satisfy Equation (6). The continuous free variables explored by the optimizer are the phase lag and shift of the wing root pitch angle, θ_r , with respect to flapping motion, ϕ_r . This method has been proven effective in our earlier effort to study energetics of hovering [16] or straight-flying animals [42].

A typical periodic cycle for forward-level flight is given in Figure 4.

At each time t , the instantaneous total power, P_{tot} , can be obtained as [18, 19]

$$P_{tot}(t) = \tau_w \dot{\mathbf{q}}_w, \quad (7)$$

where $\dot{\mathbf{q}}_w$ are the generalized velocities for the two wings and τ_w are the generalized internal forces of the wing-body system. We assume that the effect of storage and release of elastic energy in muscles and tendons in the wing is small and can be neglected—thus, only positive power will be considered in the calculation of cycle-averaged power, although there is evidence that the elastic tendon may contribute to overall energetics in flying vertebrates [46, 47]. A similar argument was made by Bahlman et al. [48] and Fan et al. [9]—both of them built robotic wings to emulate bat flight, and considered only the work done by the motor in estimating flight power.

3 | Results

3.1 | Quasi-Steady Aerodynamic Model at Moderate Reynolds Numbers

The lift and drag coefficients as a function of the angle of attack are presented in Figure 3A and B, respectively, where the lift and drag coefficients are defined as

$$C_L = 2L/\rho_f U^2 ch, \quad (8)$$

$$C_D = 2D/\rho_f U^2 ch. \quad (9)$$

The lift and drag coefficients are well approximated by the following empirical relationships in terms of the angle of attack, α (in degrees):

$$C_L(\alpha) = -0.44e^{-0.47\alpha} + 1.19 \sin(1.74\alpha + 20^\circ), \quad (10)$$

$$C_D(\alpha) = 1.04 + \sin(1.72\alpha - 70^\circ), \quad (11)$$

where, in each case, the best-fit regression curve with a 95% confidence interval yielded an R-squared value greater than 0.995. As illustrated in Figure 3A, the C_L curve follows closely the steady thin airfoil theory prediction with a slope of $d C_L / d \alpha = 2\pi$ at small angles of attack ($\alpha < 8^\circ$). Upon the attainment of maximum lift coefficient at approximately $\alpha \approx 40^\circ$, the lift curve decays monotonically as α is further increased. Experimental data from the literature are compared with the results of the current study. While the low Reynolds number quasi-steady model by Dickinson et al. [11] (orange curve) under predicts the lift at small angles of attack ($\alpha < 13^\circ$) and over predicts it at large angles of attack ($13^\circ < \alpha < 90^\circ$), the datasets from Pelletier and Mueller [49]; Okamoto and Azuma [50]; Nudson et al. [51] exhibit a good agreement to the current study at small angles of attack ($\alpha < 8^\circ$). Among them, the measurements from Okamoto and Azuma [50] closely follow the trend observed in our study across the full range of angles (0–90°), though their force coefficients are consistently slightly lower than those reported in our study at large angles of

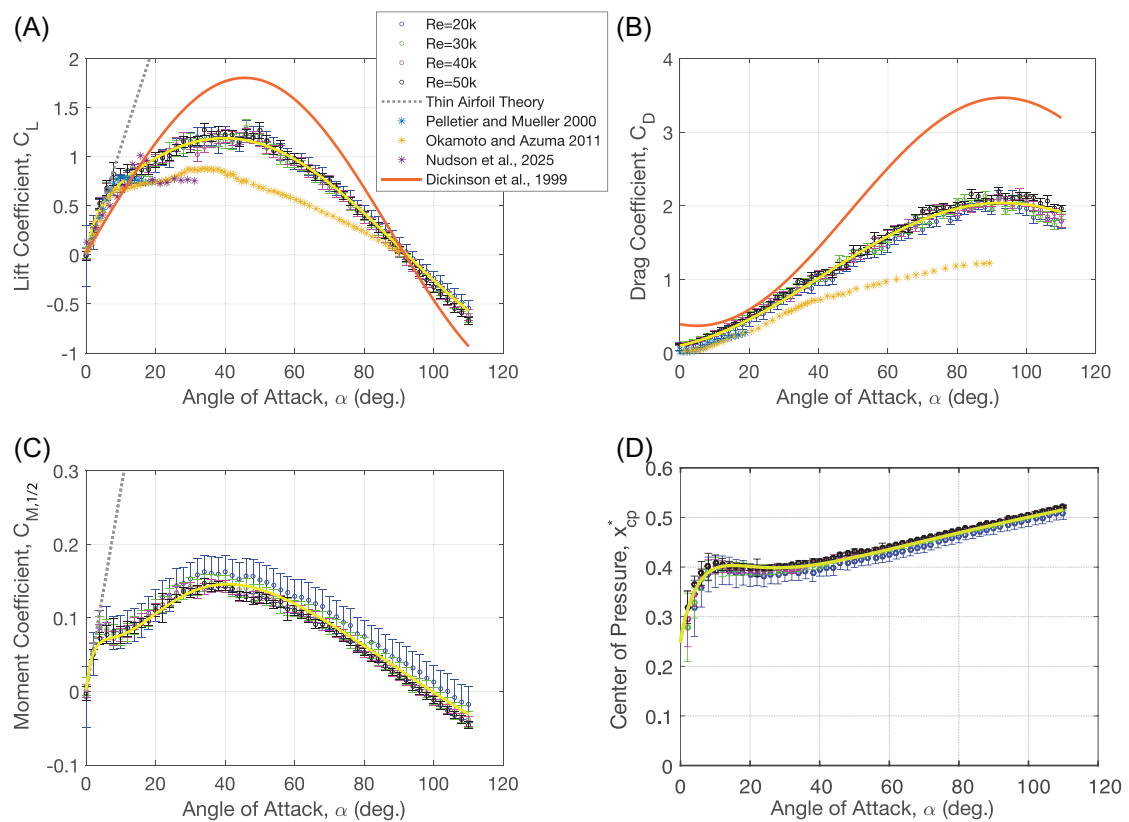


FIGURE 3 | The evolution of normalized lift (A), drag (B), moment about the mid chord (C), and center of pressure (D) as a function of the angle of attack, α , at four distinct Reynolds numbers. The error bar associated with each data point represents the standard deviation of the time-averaged measurement. Thin airfoil theory predictions of lift coefficient (i.e., $2\pi\alpha$) and moment coefficient (i.e., $\frac{\pi}{2}\alpha$) are plotted with the gray dotted lines in (A) and (C), respectively. The current study is compared with literature using similar experimental conditions [11, 49–51]. The regression curves for C_L , C_D , and x_{cp}^* are plotted with the solid yellow curves, where the corresponding equations are provided in Equations (10), (11), and (13)]. The regression curve for moment coefficient is deduced analytically using the expressions of C_L , C_D , and x_{cp}^* (discussed further in the text).

attack ($\alpha > 8^\circ$). This difference is likely attributable to the thin plate (thickness ratio $< 1.7\%$) used in the literature compared to the thicker airfoil with end plates employed in our current experiments. Prior research [52] indicates that thicker airfoils tend to achieve higher maximum lift coefficients at large angles of attack. In addition, Okamoto and Azuma [50] also reported a specific Reynolds number range ($5800 < Re < 13,000$), in which nonlinear behavior in the lift coefficient (C_L increases when Re drops) was observed at small angles of attack ($5^\circ < \alpha < 8^\circ$) for high-aspect-ratio elliptical foils (AR = 6). In the present study, the Reynolds number range extends beyond the specific range reported by Okamoto and Azuma [50], and as a result, the nonlinearities in lift coefficient were not observed.

In Figure 3B, the drag coefficient increases monotonically from approximately 0.1 at $\alpha = 0$ to a maximum value of 2.0 at $\alpha \approx 90^\circ$. Although it follows a similar trend, the data in the current study lie either below the low-Reynolds number model (orange curve) or above the data reported in the literature (blue and yellow dots).

The pitching moment coefficient, $C_{M,1/2}$, about the mid chord $c/2$,

$$C_{M,1/2} = \frac{M}{0.5\rho_f U^2 c^2 h}, \quad (12)$$

is shown in Figure 3C. In particular, the $C_{M,1/2}$ curves show a slope of $d C_M / d \alpha = \pi/2$ at small angles of attack, closely following the steady thin airfoil theory prediction.

Finally, the evolution of center of pressure, x_{cp}^* , as a function of α is illustrated in Figure 3D at four distinct Reynolds numbers. We can see that all four cases collapse well. An empirical fit of center of pressure, x_{cp}^* , is given by

$$x_{cp}^*(\alpha) = 0.247 + 0.016\alpha^{0.6} + 0.026\alpha e^{-0.11\alpha}, \quad (13)$$

which is the yellow solid curve in Figure 3D. One can evidently infer that the current model predicts that x_{cp}^* approaches the aerodynamic center at 0.25 (quarter chord) in the limit as α tends to zero, which agrees well with the linear inviscid theories [53–55]. The predicted x_{cp}^* is close to, but not exactly 0.5 when the angle of attack approaches 90° , which is likely due to experimental uncertainties in the moment measurements.

With the knowledge of center of pressure, the moment coefficient, C_M , about any arbitrary point can be easily approximated using Equations (10), (13) and

$$C_M = C_N(x^* - x_{cp}^*), \quad (14)$$

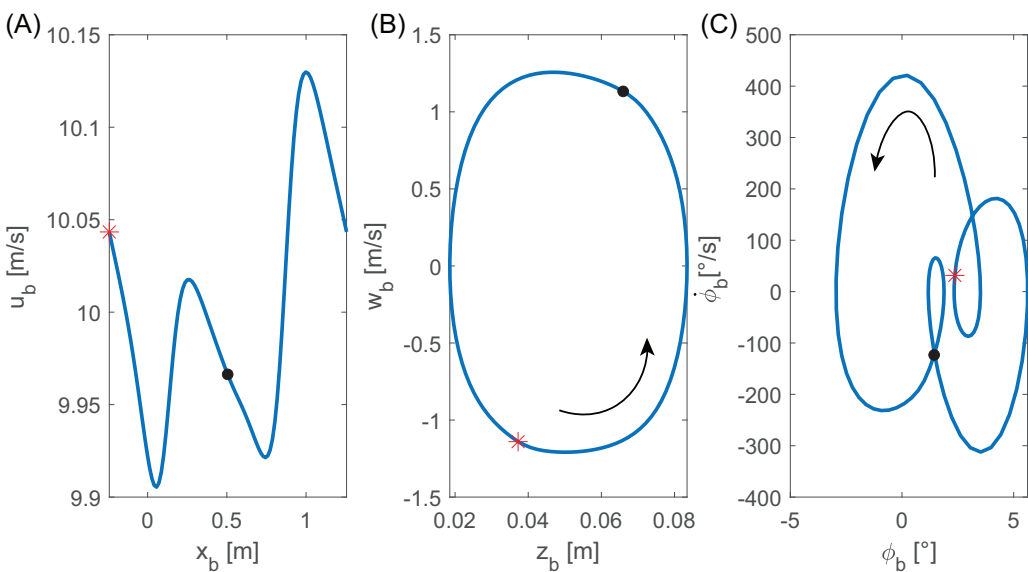


FIGURE 4 | A sample periodic orbit of the flapping wing dynamical system. The motion of the wing-body systems—vertical displacement and body pitching angle are cyclic, but there is net accumulation in the forward direction. (A) Horizontal velocity, u_b , and displacement, x_b ; (B) vertical velocity, w_b , and displacement, z_b ; (C) body pitch velocity $\dot{\phi}_b$, and pitch angle, ϕ_b . Asterisk represents beginning of downstroke, and black solid circle represents beginning of upstroke. The black arrows indicate the direction of time. The average flight speed is $U = 10 \text{ m/s}$.

where C_N is the normal force coefficient, defined as $C_N = C_L \cos(\alpha) + C_D \sin(\alpha)$, which is the measured normal force coefficient of F_N , and x^* denotes the arbitrary location of the moment axis with respect to the leading edge (e.g., $x^* = 0.25$ for the quarter-chord point).

3.2 | Application in Modeling Bird and Bat Flight

Using the aerodynamic models from Dickinson et al. [11] and current study (Equations 10 and 11), we apply our dynamic model (Equation 5) to simulate the forward flight of an idealized pigeon and bat, as described earlier. Given a flight speed, the computational model finds the minimum possible flapping frequency among all candidate wing kinematics. Animals tend to find power-optimal kinematics to fly [56, 57], and it has been demonstrated that the flapping frequency, being a simple scalar value, closely corresponds to optimal energy solution for hovering animals [16]. In addition, compared to the direct measurement of power required to fly, flapping frequency is a more accessible observation that has been well documented by biologists over the years, thus serving as a good metric to compare against [43, 44]. Given a target flight speed, the lower flapping frequency means the animal would travel further during one wingbeat cycle, and is visually compared in Figure S1. A sample solution is illustrated using phase plots in Figure 4. The forward (u_b), vertical (w_b) velocities and body pitching rate ($\dot{\phi}_b$) vary within a cycle, and because the target speed is level and straight, the phase plots of w_b - z_b and $\dot{\phi}_b$ - ϕ_b form closed loops. In contrast, the phase plot of u_b - x_b does not form a closed loop, reflecting the forward translation.

We then vary the prescribed flight speed to study how the aerodynamic models impact the optimized flapping frequency over a range of physically plausible speeds (Figure 5). For the flight of a pigeon in Figure 5A, at high forward velocities ($U > 10 \text{ m/s}$),

the aerodynamic model in the current study (blue dots) gradually converges to the measured wingbeat frequencies (green dots) by Tobalske and Dial [43], while the formulations of Dickinson et al. [11] (red dots) predict almost twice as much of flapping frequency and the discrepancy is seen to increase with flight speed. For the flight of a bat (Figure 5B), at low forward speeds ($U < 5 \text{ m/s}$), the two models predict similar flapping frequency, but as the flight speed picks up ($U > 5 \text{ m/s}$), the difference in frequency between the two models becomes much more pronounced. The species of bat considered here typically fly with a constant flapping frequency around 6 Hz [44] and are invariant of flight speed. The predicted flapping frequency given by our proposed model agrees very well with recorded observation data, especially around $U = 5\text{--}10 \text{ m/s}$, although at higher flight speed, the simulation would still deviate from measured flapping frequency.

Fundamentally, the predicted differences in flapping frequency are manifestation of different aerodynamic forces experienced by the wings. We choose a representative case of $U = 10 \text{ m/s}$ for the bat flight in Figure 6 to illustrate the evolution of forces due to the different aerodynamic models. The new aerodynamic model (Equations 10 and 11) predicts smaller effective angles of attack for both inboard (1/4-span) and outboard (3/4-span) of the wing, and as a result, smaller horizontal and vertical forces are observed.

Another important distinction between the two aerodynamic models concerns flight energetics. We compared the sum of joint forces τ_w (the internal forces between the wing and the body, in Equation 7) in Figure 7A for a case of bat flight at speed $U = 10 \text{ m/s}$. The predicted joint torques from Dickinson and Sane model are consistently higher than that obtained from our proposed model, as a result of overprediction in flapping frequency, and in Figure 7B, their model results in a maximum power of 150 W (mass-specific power $\sim 2000 \text{ W kg}^{-1}$), whereas the proposed model predicts a peak power of 30 W ($\sim 400 \text{ W kg}^{-1}$), which

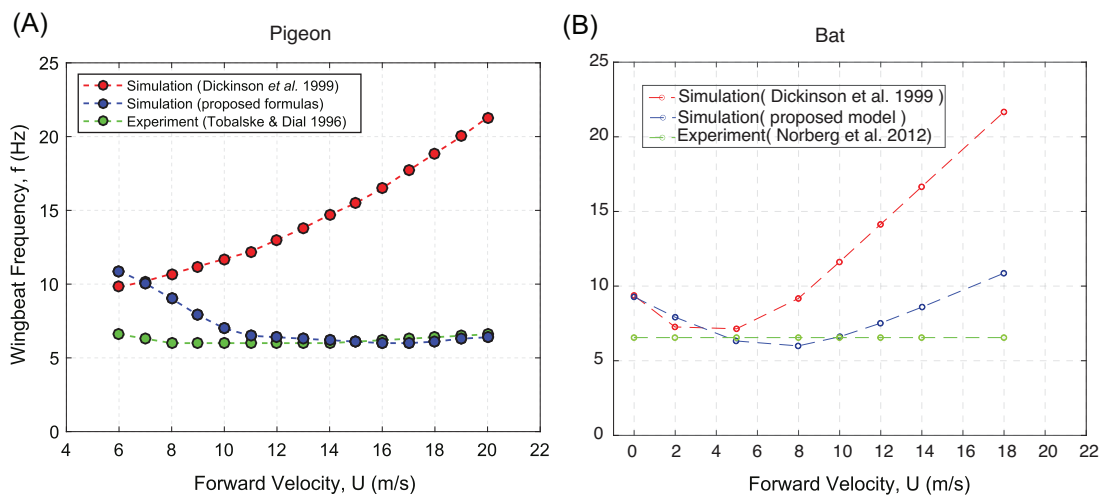


FIGURE 5 | Predicted flapping frequency of (A) a pigeon and (B) a bat as a function of flight speed. The dashed green line is experimentally measured flapping frequency. Red dots represent the wingbeat frequencies evaluated using the quasi-steady aerodynamic formulations of Dickinson et al. [11]. Blue dots designate the predicted wingbeat frequencies using the proposed aerodynamic formulas. Only the aerodynamic models are different between the two simulations.

falls more reasonably in the range of metabolic power available to animals [58].

One important aspect that relates to applications in aerial robotics is the body pitching angle variation within a cycle—which may impact onboard camera measurement, inertia measurement unit sensoring, thus detrimentally impacting the state estimation. Animals typically fly with a stable body orientation that varies only a few degrees [17]. In Figure 8, we see the range of pitching angles using Dickinson and Sane model, which can be as large as 25 degrees, whereas the current model bounds the pitching variation within 10 degrees. A direct visual comparison can be found in Figure S1, where we see the body pitch angle is much more pronounced during upstroke.

Finally, the simulations conducted here serve to highlight the effectiveness of the aerodynamic model at high Reynolds number, and thus, the results should not be interpreted as the exact wing kinematics animals would adopt. More specifically, we only considered pigeon wings to retract and highly articulate bat wings to twist and folding, but, in reality, both animals would likely have all three motions and likely more, such as wing sweeping [59] and dynamic camber [18]. However, the underlying message remains strong—that our aerodynamic model at high Reynolds number is more effective in supporting the quasi-steady simulation. Concretely, we simulated the physical morphological parameters (wingspan, weight, chord, etc.) with bat wing kinematics (which performs twist and folding), under two different wind speeds ($U = 5$ and 18 m/s , corresponds to low and high Re , respectively, see Table 1), and we found that while the exact frequencies predicted may be different, our proposed model would predict a lower flapping frequency at high Re , and slightly higher frequency at low Re —consistent with what is being reported in Figure 5B, even if the bat wing kinematics were now applied to pigeon morphology. In addition, to test how wing geometry may affect the result, we varied the aspect ratio of the wing ($AR = S/b$, where S is the wing surface area and b is the wingspan), and again, the result confirms that while the

TABLE 1 | Sensitivity to wing geometry (AR, aspect ratio), using pigeon morphology with bat kinematics.

Case	AR	U	Dickinson et al.	Proposed model
1	5	18	21.3	12.6
2	5	5	12.6	15.5
3	6	18	16.1	15.3

difference in predicted frequency shrinks, our proposed model still yields a lower flapping frequency.

4 | Discussion

4.1 | Aerodynamic Forces at Moderate Reynolds Number

In the current study, the aerodynamic forces of a rectangular foil are characterized at a series of angles of attack over a range of Reynolds numbers ($Re = 20,000\text{--}50,000$). The magnitudes of lift coefficient, C_L , and drag coefficient, C_D , are found to be comparable to those obtained from steady-state force measurements of a pitching flat plate ($Re = 20,000$) [60] and from measurements on a translating two-dimensional rectangular wing at various fixed angles of attack ($Re \sim 200$) [10]. The peak of lift coefficient, C_L in Figure 3A, is achieved at around 40° in the current study, which is also in line with experimental studies using flat plates ($\sim 35^\circ$ [50], $\sim 40^\circ$ [10], and $\sim 45^\circ$ [60]), insect wing models ($\sim 45^\circ$ [11]), and a dried pigeon wing ($\sim 40^\circ$ [35]).

The maximum drag coefficient, C_D in Figure 3B, conforms very well with the theoretical prediction of 1.95, wherein the drag coefficient associated with a two-dimensional flat plate facing perpendicular to the incoming flow can be approximated as $C_D = 1.95 + 50/Re$ [61]. The rough shape of the drag coefficient (C_D) in the current study is well approximated with a simple har-

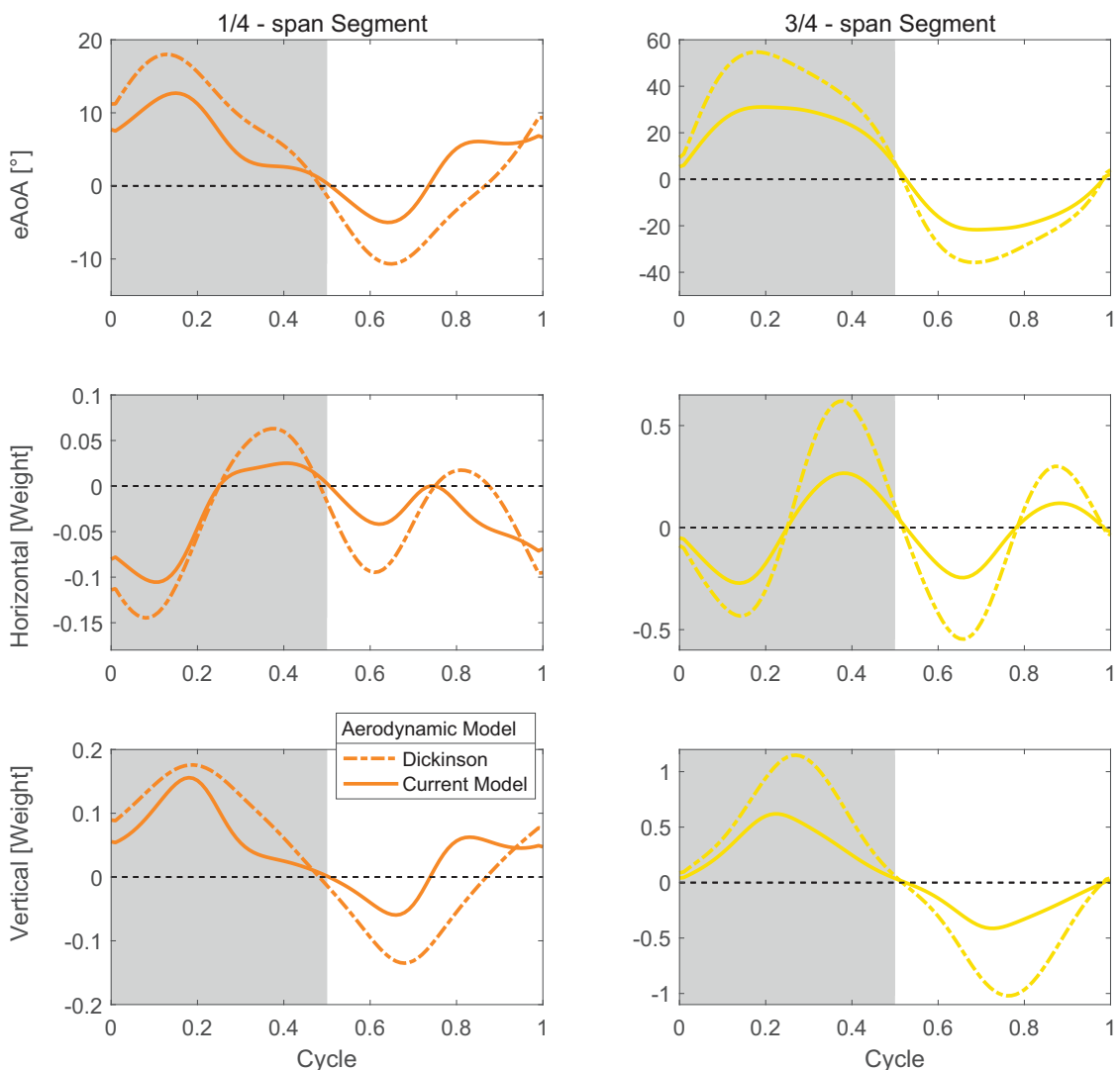


FIGURE 6 | Effective angles of attack, horizontal and vertical forces produced by 1/4 and 3/4-span wing segments. The freestream $U = 10$ m/s, and the dashed and solid lines are time series using aerodynamic models proposed by Dickinson et al. [11] and the current study (Equation 10), respectively. The shaded area represents downstroke. The forces are normalized by the weight of the animal, and the time is normalized by one flapping period.

monic relationship, and resembles the functional form derived in the experimental work of Dickinson et al. [11], where steady-state translational force measurements (i.e., C_L and C_D) were conducted on a dynamically scaled-up *Drosophila* wing at a Reynolds number of approximately 140, much smaller than that in the current study ($Re = 20,000\text{--}50,000$).

However, the general characteristics of the present force profiles differ conspicuously from those of Dickinson et al. [11]. First, the slope of our C_L values conforms with the thin airfoil theory predictions for small angles. Dickinson et al. [11] largely underestimate the theoretical prediction of $dC_L/d\alpha = 2\pi$ with a value of approximately 3.8. This discrepancy is likely due to the experiments in Dickinson et al. [11] surveyed a low Re of $\mathcal{O}(10^2)$, which does not satisfy the inviscid flow assumption—the basis of the thin airfoil theory [62]. Second, the maximum C_L and C_D obtained in the present study are approximately 45% and 65% smaller, respectively. Higher steady-state aerodynamic forces associated with a rotating 3D wing are due, in part, to the formation, growth, and subsequent stabilization of an attached LEV on the upper

surface (or suction/dorsal side, used synonymously) of the wing, as previously noted by a number of investigators [11, 25, 63]. The general consensus in the archival literature is that the parameter of rotation (e.g., revolving, flapping, and pitching) plays an important role in the formation and subsequent stabilization of the LEV [64–66], and that this enhanced vortex stability is directly correlated to the generation of strong aerodynamic forces [60, 67–69] and pitching moments [66, 70, 71] that far exceed their static counterparts, easily by a factor of 1.5 to 2.5 in magnitude.

Indeed, the fundamentals of vortex dynamics hold the key to understand the differences of the maxima presented by the two studies. Gharib et al. [72] used a piston-cylinder apparatus to study vortex formation, and quantitatively recorded that the vortex core will “saturate” in strength, and reject additional vorticity from the shear layer, after a nondimensional timescale, coined as the formation time $\hat{T} = UT/D$, exceeds a critical value, where U is the freestream velocity, T is the time it takes for a complete vortex ring to shed, and D is the characteristic length. For the cylinder apparatus, the vortex sheds or “pinches off” after $\hat{T} = 4$.

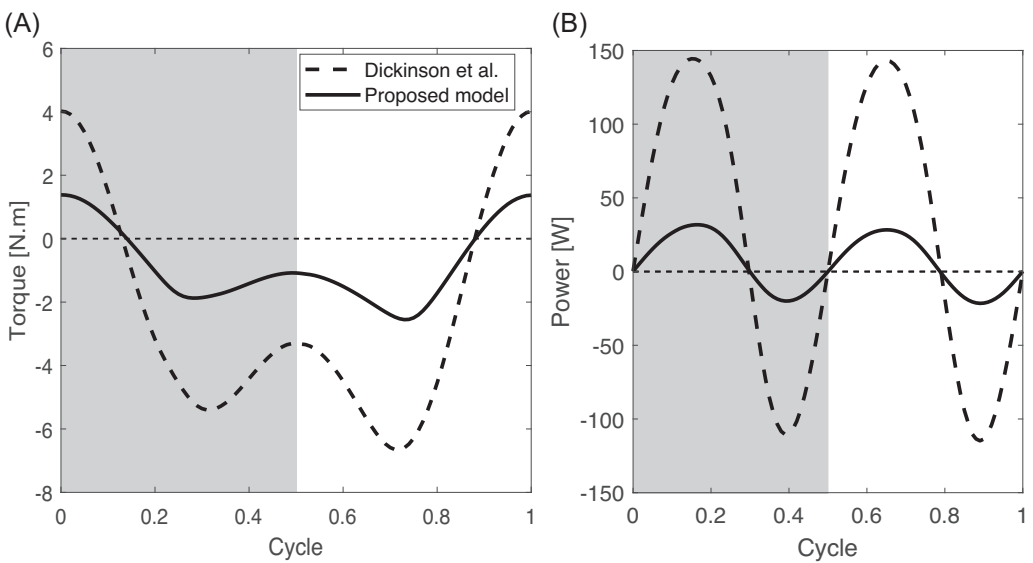


FIGURE 7 | Predicted total power for one cycle at forward flight speed of $U = 10$ m/s. Dashed and solid lines represent results using models from Dickinson et al. [11] and current study, respectively. Shaded area represents downstroke. Time is normalized by one flapping period.

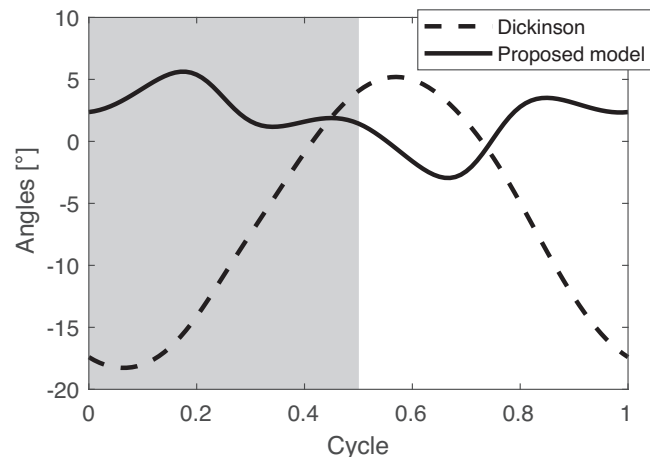


FIGURE 8 | Predicted body pitching angle variation within one cycle. Shaded area represents downstroke.

Some constant correction may be needed for other geometries than the cylinder [73]. Dickinson et al. [11] clearly demonstrated the presence of LEV, and the spanwise flow is produced by the flapping of wings, but our 2D case has no spanwise flow. Indeed, Ellington et al. [25] first observed the spanwise flow in flapping wing flight of $Re \sim 10^3$, which would transport additional vorticity outboard before finally being convected to wake as part of tip vortex, thus stabilizing the LEV (no saturation of vorticity) on the dorsal side during downstroke. Lentink and Dickinson [74] then demonstrated that this stabilizing mechanism for LEV holds for a much wider range of $Re \sim 10^2 - 10^5$ – touching on the lower Re range of this study. Later, Harbig et al. [67] found that high aspect ratio wing (the extreme is a 2D wing like ours) features reduced LEV circulation, and thus less lift coefficients. In our study, the wing is of high aspect ratio, and has an end plate to reduce tip effects, and thus, the experiment is more close to a two-dimensional flow (infinite AR) without spanwise flow, so the LEV is likely become unstable and shed much earlier than Dickinson

et al. [11], where their experiment features a rotating flapping wing with finite AR at $Re = 10^2$, with spanwise flow convecting extra vorticity outboard to tip vortex, and thus delay the shedding of LEV, which contributes to higher peak C_L and C_D .

It should be noted that the forces measured in the present study are “quasi-steady” such that the concomitant shedding of von Kármán vortices behind the plate does not induce any measurable time-dependency in the forces and the pitching moment imparted on the wing. This is presumably true because the formation of these large-scale vortices occurs in the far-wake region approximately 1.5–2 chord lengths downstream of the plate (for Reynolds numbers on the order of $\mathcal{O}(10^4) \sim \mathcal{O}(10^5)$), as discussed in Onoue and Breuer [66], and Liu et al. [75]. The validity of the present assertion is also supported by small standard deviations associated with the force and moment data presented in Figure 3, reflecting minor unsteadiness in the measurements.

This study also contributes a simple empirical relationship between the center of pressure’s location and the angle of attack. Han et al. [38] was one of the early studies to demonstrate the importance to consider variation in center of pressure using quasi-steady modeling. By simulation of a hawkmoth scale hovering flight ($Re \sim 10^2$), they observed a more consistent periodic flight characteristics when the center of pressure of the insects’ wing is allowed to be a function of angle of attack. In a much higher $Re \sim 10^5$, using recorded wing kinematics, Windes et al. [37] compared simulated bat flight trajectory with that of the measured during experiment. They considered the wing-body system only as a point mass without orientation, thus pitch dynamics was neglected. They reported that the simulation under-predicted significantly in the streamwise (forward) direction. Later, Fan and Breuer [76] modeled the bat wing-body system as a three-rigid-body system (two wings and a fuselage), each having translational as well as rotational DoF, and the simulation agrees much better with actual measured trajectory in all 6 DoF. The improvement, especially in the streamwise direction, is likely due

to the incorporation of pitching motion, as in a cycle-averaged manner, lift force tilts slightly forward due to pitching motion, thus increasing thrust, and the simulated bat “catches up” in the flight direction. The formulation to accurately capture center of pressure, which impacts the pitching moment, may thus serve as an importance for modeling high Re case.

Note that for both Han et al. [38] ($Re \sim 10^2$) and present study ($Re \sim 10^5$) (Figure 3D), the center of pressure starts around quarter-chord at small angle of attack α , which agrees well with thin airfoil theory [62].

4.2 | Animal Flight Simulations and Energetics

Equipped with the proposed model, which is suitable for moderate to high Re , the resulting flapping frequency of both the pigeons and the bats in the simulations is closer to experimental measured values (Figure 5). The difference between measured and simulation rises from unmodeled forces, which might include the unsteady aerodynamic forces due to vortex shedding and formation, finer wing muscle actuation, such as dynamic camber. The fixed flapping frequency that is invariant of flight speed is often observed in live animal flight, as animals modulate their flight speed by more localized and precise control of their wings, such as armwing camber control, handwing twisting, and folding [18].

The average lift over a cycle has to equal the weight of the animal, and thrust must balance drag to achieve forward and level flight. Using the proposed aerodynamic model in the current study, extra lift coefficient is available at small angle of attack $\alpha = 0 \sim 13^\circ$ (Figure 3A) with small penalty of drag (Figure 3B)—in other words, our proposed model features a high C_L/C_D regime for small α . As a result, our algorithm found a solution where the armwing requires minimal pitching to leverage these advantages, which manifests as a smaller effective angle of attack throughout the cycle (solid line in top left panel of Figure 6). In a loose language, the armwing segments feature a small nose-up pitch throughout the cycle, which generates lift with small drag penalty. On the other hand, when the Dickinson and Sane low Reynolds model [11] is applied at this high Reynolds scenario (pigeon or bat flight), both C_L and C_D are small within this range of angle of attack ($\alpha = 0 \sim 13^\circ$). Consequently, the algorithm can only rely on a larger α (dashed line in top left panel of Figure 6) to generate the required lift, resulting in a higher drag penalty. The outboard wing segment (3/4-span) is further away from wing root, and has a larger velocity due to flapping motion compared to inboard wing, thus having a larger α compared to inboard wing segment (1/4-span), and would not utilize the small α (or high C_L/C_D value) “perk,” which is true for either model (see Figure 2B).

Interestingly, Shyy et al. [1] pointed out that armwing (represented as 1/4-span wing segment) is mainly responsible for lift generation, and handwing (3/4-span wing segment) for thrust. This statement is supported by our simulation using both aerodynamic models. In Figure 6, we indeed see that the armwing generates a net positive lift compared to the handwing, and that for horizontal force, the armwing features more drag.

The significance of the current proposed model is also evident in the power consumption. Both CFD study by Windes et al. [37] and quasi-steady modeling by Fan et al. [18] of similar sized live bats flight show instantaneous power consumption < 4 W, which is lower than that predicted by either of the two aerodynamic models (Figure 7). This overprediction is expected as both studies used high-fidelity wing kinematics of live animals, which include more pronounced and detailed wing articulation than the much simplified kinematics considered in this paper. Our proposed model nevertheless provides a much closer power prediction compared to Dickinson and Sane model. Note that around $U = 10$ m/s, their model predicted almost twice as much flapping frequency in Figure 5, and because power roughly scales quadratically with flapping frequency [18], the instantaneous power is thus four times larger (Figure 7).

It is noteworthy that bats typically have a very small body pitching variation in flight, only by a few degrees [76], which is captured with our proposed model. In our simulation, the wings are modeled as rigid bodies with moment of inertia; thus, its rotation will, in turn, have an effect on body pitch dynamics (through the internal forces τ in Equation 5). The amplitude of the wing rotation, θ_r , is fixed to reflect the physical constraints that birds or bats shoulder joint have limitations of rotational range. Thus, the gentler body pitch motion is primarily due to the extra lift with small drag penalty at small angle of attack, allowing the wing to generate sufficient cycle-averaged lift and maintain thrust-drag balance. As a result, the body does not need to oscillate as violently, so the wing may reach large angle of attack (top left and right panels in Figure 6).

Finally, it is important to highlight that the differentiable nature of the proposed formulas makes them highly suitable to be used in dynamical simulations that utilize gradient-based optimization techniques to determine, for example, power-optimal kinematics of avian wings for different modes of flight.

Author Contributions

Y.S., X.F., K.O., and H.V. drafted the paper; Y.S., K.O., and H.V. designed and executed the experiments; K.O. characterized the aerodynamic models; X.F. and H.V. performed numerical simulations, K.S.B. supervised and managed the project, reviewed and edited the draft, and acquired financial support on the project.

Acknowledgments

The authors would like to thank the members of the Energy Harvesting group at Brown University for their contributions to the development of the experimental apparatus.

Conflicts of Interest

The authors declare no competing financial interests.

Funding

The original experiments were supported by the Department of Energy’s Advanced Research Projects Agency-Energy (ARPA-E), Grant No. DE-AR0000318. Subsequent data analysis and manuscript preparation were supported by NSF Grant IOS-1930924 and ONR Grant N00014-21-1-2816.

References

1. W. Shyy, H. Aono, C.-K. Kang, and H. Liu, *An Introduction to Flapping Wing Aerodynamics* (Cambridge University Press, 2013), <https://doi.org/10.1017/cbo9781139583916>.
2. W. Shyy, C.-K. Kang, P. Chirarattananon, S. Ravi, and H. Liu, "Aerodynamics, Sensing and Control of Insect-Scale Flapping-Wing Flight," *Proceedings of the Royal Society A: Mathematical, Physical and Engineering Science* 472, no. 2186 (2016): 20150712, <https://doi.org/10.1098/rspa.2015.0712>.
3. T. J. Mueller, "Fixed and Flapping Wing Aerodynamics for Micro Air Vehicle Applications," in *AIAA* (2001).
4. Z. J. Wang, "Dissecting Insect Flight," *Annual Review of Fluid Mechanics* 37 (2005): 183–210.
5. S. Ansari, R. Źbikowski, and K. Knowles, "Aerodynamic Modelling of Insect-Like Flapping Flight for Micro Air Vehicles," *Progress in Aerospace Sciences* 42, no. 2 (2006): 129–172.
6. W. Shyy, Y. Lian, J. Tang, D. Viieru, and H. Liu, *Aerodynamics of Low Reynolds Number Flyers* (Cambridge University Press, 2008).
7. H. E. Taha, M. R. Hajj, and A. H. Nayfeh, "Flight Dynamics and Control of Flapping-Wing MAVS: A Review," *Nonlinear Dynamics* 70 (2012): 907–939.
8. X. Fan, A. Gehrke, and K. Breuer, "Wing Twist and Folding Work in Synergy to Propel Flapping Wing Animals and Robots," in *IEEE/RSJ International Conference on Intelligent Robots and Systems* (2024), <https://arxiv.org/abs/2408.15577>.
9. X. Fan, A. Bortoni, S. Hao, S. Swartz, and K. Breuer, "Upstroke Wing Clapping in Bats and Bat-Inspired Robots Offers Efficient Lift Generation," *Journal of the Royal Society Interface* 22, no. 223 (2025): 20240590, <https://doi.org/10.1098/rsif.2024.0590>.
10. M. H. Dickinson and K. Götz, "Unsteady Aerodynamic Performance of Model Wings at Low Reynolds Numbers," *Journal of Experimental Biology* 174 (1993): 45–64, <https://doi.org/10.1242/jeb.00739>.
11. M. H. Dickinson, F. O. Lehmann, and S. P. Sane, "Wing Rotation and the Aerodynamic Basis of Insect Right," *Science* 284, no. 5422 (1999): 1954–1960, <https://doi.org/10.1126/science.284.5422.1954>.
12. S. P. Sane and M. H. Dickinson, "The Control of Flight Force By A Flapping Wing: Lift and Drag Production," *Journal of Experimental Biology* 204, no. 15 (2001): 2607–2626, , <http://jeb.biologists.org/content/204/15/2607>.
13. S. P. Sane and M. H. Dickinson, "The Aerodynamic Effects of Wing Rotation and A Revised Quasi-Steady Model of Flapping Flight.,," *Journal of Experimental Biology* 205, no. Pt 8 (2002): 1087–1096, <https://doi.org/10.1126/science.167.3915.177>.
14. G. J. Berman and Z. J. Wang, "Energy-Minimizing Kinematics in Hovering Insect Flight," *Journal of Fluid Mechanics* 582 (2007): 153–168.
15. T. L. Hedrick and T. L. Daniel, "Flight Control in the Hawkmoth Manduca Sexta: The Inverse Problem of Hovering," *Journal of Experimental Biology* 209, no. 16 (2006): 3114–3130.
16. H. R. Vejdani, D. B. Boerma, S. M. Swartz, and K. S. Breuer, "The Dynamics of Hovering Flight in Hummingbirds, Insects and Bats With Implications for Aerial Robotics," *Bioinspiration and Biomimetics* 14, no. 1 (2018): 016003, <https://doi.org/10.1088/1748-3190/aaea56>.
17. X. Fan and K. Breuer, "Low-Order Modeling of Flapping Flight With Highly Articulated, Cambered, Heavy Wings," *AIAA Journal* 60 (2021): 1–10, <https://doi.org/10.2514/1.J060661>.
18. X. Fan, S. Swartz, and K. Breuer, "Power Requirements for Bat-Inspired Flapping Flight With Heavy, Highly Articulated and Cambered Wings," *Journal of the Royal Society, Interface* 19, no. 194 (2022): 20220315, <https://doi.org/10.1098/rsif.2022.0315>.
19. B. Parslew, "Predicting Power-Optimal Kinematics of Avian Wings," *Journal of the Royal Society Interface* 12, no. 102 (2015): 20140953, <https://doi.org/10.1098/rsif.2014.0953>.
20. B. Parslew and W. J. Crowther, "Simulating Avian Wingbeat Kinematics," *Journal of Biomechanics* 43, no. 16 (2010): 3191–3198, <https://doi.org/10.1016/j.jbiomech.2010.07.024>.
21. B. Cheng, B. W. Tobalske, D. R. Powers, et al., "Flight Mechanics and Control of Escape Manoeuvres in Hummingbirds II. Aerodynamic Force Production, Flight Control and Performance Limitations," *Journal of Experimental Biology* 219 (2016): 3518–3531.
22. D. D. Chin and D. Lentink, "Flapping Wing Aerodynamics: From Insects to Vertebrate," *Journal of Experimental Biology* 219 (2016): 920–932.
23. J. Song, H. Luo, and T. L. Hedrick, "Comparison Of CFD And Quasi-Steady Analysis Of Hovering Aerodynamics For A Ruby-Throated Hummingbird," in 32nd AIAA Applied Aerodynamics Conference (2014), 2149.
24. C. Ellington, "Insects Versus Birds: The Great Divide," in 44th AIAA Aerospace Sciences Meeting and Exhibit (2006), 35.
25. C. P. Ellington, C. van den Berg, A. Willmott, and A. L. R. Thomas, "Leading-Edge Vortices in Insect Flight," *Nature* 384 (1996): 626–630.
26. J. R. Usherwood and C. P. Ellington, "The Aerodynamics of Revolving Wings I. Model Hawkmoth Wings," *Journal of Experimental Biology* 205, no. 11 (2002): 1547–1564.
27. J. R. Usherwood and C. P. Ellington, "The Aerodynamics of Revolving Wings II. Propeller Force Coefficients From Mayfly to Quail," *Journal of Experimental Biology* 205, no. 11 (2002): 1565–1576.
28. E. Anderson and E. Demont, "The Mechanics of Locomotion in the Squid Loligo Pealei: Locomotory Function and Unsteady Hydrodynamics of the Jet and Intramantle Pressure," *Journal of Experimental Biology* 203 (2000): 2851–2863, <https://doi.org/10.1242/jeb.203.18.2851>.
29. K. Byl, "A Passive Dynamic Approach for Flapping-Wing Micro-Aerial Vehicle Control," in *Dynamic Systems and Control Conference*, Vol. 44175 (2010), 215–223.
30. L. Chen, Y. Guan, X. Zhang, and H. Zhang, "Improvement of an Aerodynamic Model for Biomimetic Flapping-Wing Robots," in 2010 IEEE/ASME International Conference on Advanced Intelligent Mechatronics (2010), 49–54, <https://doi.org/10.1109/AIM.2010.5695882>.
31. A. K. Stowers and D. Lentink, "Folding In and Out: Passive Morphing in Flapping Wings," *Bioinspiration & Biomimetics* 10, no. 2 (2015): 025001, <https://doi.org/10.1088/1748-3190/10/2/025001>.
32. T. J. G. Read, P. S. Segre, K. M. Middleton, and D. L. Altshuler, "Hummingbirds Control Turning Velocity Using Body Orientation and Turning Radius Using Asymmetrical Wingbeat Kinematics," *Journal of the Royal Society Interface* 13, no. 116 (2016): 20160110, <https://doi.org/10.1098/rsif.2016.0110>.
33. A. C. Carruthers, A. L. Thomas, S. M. Walker, and G. K. Taylor, "Mechanics and Aerodynamics of Perching Manoeuvres in a Large Bird of Prey," *Aeronautical Journal* 114, no. 1161 (2010): 673–680.
34. A. C. Carruthers, S. M. Walker, A. L. Thomas, and G. K. Taylor, "Aerodynamics of Aerofoil Sections Measured on a Free-Flying Bird," *Proceedings of the Institution of Mechanical Engineers, Part G: Journal of Aerospace Engineering* 224, no. 8 (2010): 855–864.
35. J. R. Usherwood, "The Aerodynamic Forces and Pressure Distribution of a Revolving Pigeon Wing," *Experiments in Fluids* 46 (2009): 991–1003.
36. H. E. Taha, M. R. Hajj, and P. S. Beran, "State-Space Representation of the Unsteady Aerodynamics of Flapping Flight," *Aerospace Science and Technology* 34 (2014): 1–11.
37. P. Windes, X. Fan, M. Bender, D. K. Tafti, and R. Müller, "A Computational Investigation of Lift Generation and Power Expenditure of Pratt's Roundleaf Bat (*Hipposideros pratti*) in Forward Flight," *PLoS One* 13, no. 11 (2018): e0207613, <https://doi.org/10.1371/journal.pone.0207613>.
38. J. S. Han, J. K. Kim, J. W. Chang, and J. H. Han, "An Improved Quasi-Steady Aerodynamic Model for Insect Wings That Considers Movement of the Center of Pressure," *Bioinspiration and Biomimetics* 10, no. 4 (2015): 046014, <https://doi.org/10.1088/1748-3190/10/4/046014>.

39. Y. Su, M. Miller, S. Mandre, and K. Breuer, "Confinement Effects on Energy Harvesting By A Heaving and Pitching Hydrofoil," *Journal of Fluids and Structures* 84 (2019): 233–242.
40. Y. Su and K. Breuer, "Resonant Response and Optimal Energy Harvesting of an Elastically Mounted Pitching and Heaving Hydrofoil," *Physical Review Fluids* 4, no. 6 (2019): 064701.
41. Y. Su, *Energy Harvesting and Aeroelastic Instabilities Using Prescribed and Elastically-Mounted Pitching and Heaving Hydrofoils* (Brown University). 2019.
42. X. Fan, K. Breuer, and H. Vejdani, "Wing Fold and Twist Greatly Improves Flight Efficiency for Bat-Scale Flapping Wing Robots," in *IEEE International Conference on Intelligent Robots and Systems* (2021), <https://doi.org/10.1109/IROS5116.2021.9636735>.
43. B. Tobalske and K. Dial, "Flight Kinematics of Black-Billed Magpies and Pigeons Over A Wide Range of Speeds," *Journal of Experimental Biology* 199, no. 2 (1996): 263–280, , <http://jeb.biologists.org/content/199/2/263>.
44. U. M. Norberg and R. Åke Norberg, "Scaling of Wingbeat Frequency with Body Mass in Bats and Limits to Maximum Bat Size," *Journal of Experimental Biology* 215, no. 5 (2012): 711–722, <https://doi.org/10.1242/jeb.059865>.
45. H. Glauert, *The Elements of Aerofoil and Airscrew Theory* (Cambridge University Press, 1983).
46. A. A. Biewener, W. R. Corning, and B. W. Tobalske, "In Vivo Pectoralis Muscle Force-Length Behavior During Level Flight in Pigeons (*Columba livia*)," *Journal of Experimental Biology* 201, no. 24 (1998): 3293–3307.
47. N. Konow, J. A. Cheney, T. J. Roberts, J. R. S. Waldman, and S. M. Swartz, "Spring or String: Does Tendon Elastic Action Influence Wing Muscle Mechanics in Bat Flight?," *Proceedings of the Royal Society B: Biological Sciences* 282, no. 1816 (2015): 1–7, <https://doi.org/10.1098/rspb.2015.1832>.
48. J. W. Bahlman, S. M. Swartz, and K. S. Breuer, "Design and Characterization of a Multi-Articulated Robotic Bat Wing," *Bioinspiration & Biomimetics* 8, no. 1 (2013): 16009, <https://doi.org/10.1088/1748-3182/8/1/016009>.
49. A. Pelletier and T. J. Mueller, "Low Reynolds Number Aerodynamics of Low-Aspect-Ratio, Thin/Flat/Cambered-Plate Wings," *Journal of Aircraft* 37, no. 5 (2000): 825–832.
50. M. Okamoto and A. Azuma, "Aerodynamic Characteristics at Low Reynolds Number for Wings of Various Planforms," *AIAA Journal* 49, no. 6 (2011): 1135–1150.
51. H. Hudson, D. Stanfield-Brown, K. Bennett, and L. W. Traub, "Characterization of the Effects of Wing Sweep at Low Reynolds Number," *Journal of Aircraft* 62 (2025): 1–7.
52. S. Roy, B. Das, and A. Biswas, "Influence of Camber Ratio and Thickness Ratio on the Airfoil Performance," in *Recent Advances in Mechanical Engineering: Select Proceedings of ICRAE 2020*, (Springer, 2021), 729–737.
53. H. Wagner, "Über die Entstehung des dynamischer Austrieb von Tragflügeln," *ZAMM* 5 (1925): 17–35.
54. T. Theodorsen, "General Theory of Aerodynamic Instability and the Mechanism of Flutter," *NASA Technical Report* 496 (1935).
55. I. E. Garrick, "Propulsion of a Flapping and Oscillating Airfoil," *NASA Technical Report*, 567 (1936).
56. M. Klein Heerenbrink, L. C. Johansson, and A. Hedenström, "Power of the Wingbeat: Modelling the Effects of Flapping Wings in Vertebrate Flight," *Proceedings of the Royal Society A: Mathematical, Physical and Engineering Sciences* 471, no. 2177 (2015): 20140952, <https://doi.org/10.1098/rspa.2014.0952>.
57. K. C. Hall and S. R. Hall, "Minimum Induced Power Requirements for Flapping Flight," *Journal of Fluid Mechanics* 323 (1996): 285–315, <https://doi.org/10.1017/S0022112096000924>.
58. C. P. Ellington, "Limitations on Animal Flight Performance," *Journal of Experimental Biology* 160, no. 1 (1991): 71–91, <https://doi.org/10.1242/jeb.160.1.71>.
59. B. Parslew, "Simulating Avian Wingbeats and Wakes," Ph.D. thesis, University of Manchester (2012).
60. K. O. Granlund, M. V. Ol, and L. P. Bernal, "Unsteady Pitching Flat Plates," *Journal of Fluid Mechanics* 733 (2013): R5, <https://doi.org/10.1017/jfm.2013.444>.
61. C. P. Ellington, "Aerodynamics and the Origin of Flight," *Advances in Insect Physiology* 23 (1991): 171–210.
62. R. L. Bisplinghoff, H. Ashley, and R. L. Halfman, *Aeroelasticity* (Addison-Wesley Publishing Co. Inc., 1957).
63. T. Maxworthy, "The Fluid Dynamics of Insect Flight," *Annual Review of Fluid Mechanics* 13 (1981): 329–350.
64. D. Lentink and M. H. Dickinson, "Biofluid Dynamic Scaling of Flapping, Spinning, and Translating Fins and Wings," *Journal of Experimental Biology* 212 (2009): 2691–2704.
65. J. G. Wong and D. E. Rival, "Determining the Relative Stability of Leading-Edge Vortices on Nominally Two-Dimensional Flapping Profiles," *Journal of Fluid Mechanics* 766 (2015): 611–625.
66. K. Onoue and K. S. Breuer, "Vortex Formation and Shedding From a Cyber-Physical Pitching Plate," *Journal of Fluid Mechanics* 793 (2016): 229–247, <https://doi.org/10.1017/jfm.2016.134>.
67. R. R. Harbig, J. Sheridan, and M. C. Thompson, "Reynolds Number and Aspect Ratio Effects on the Leading-Edge Vortex for Rotating Insect Wing Planforms," *Journal of Fluid Mechanics* 717 (2013): 166–192.
68. B. L. R. Ribeiro, Y. Su, Q. Guillaumin, K. S. Breuer, and J. A. Franck, "Wake–Foil Interactions and Energy Harvesting Efficiency in Tandem Oscillating Foils," *Physical Review Fluids* 6, no. 7 (2021): 074703.
69. S. Ōtomo, S. Henne, K. Mullenens, K. Ramesh, and I. M. Viola, "Unsteady Lift on a High-Amplitude Pitching Aerofoil," *Experiments in Fluids* 62 (2021): 1–18.
70. K. Onoue, A. Song, B. Strom, and K. Breuer, "Large Amplitude Flow-Induced Oscillations and Energy Harvesting Using A Cyber-Physical Pitching Plate," *Journal of Fluids and Structures* 55 (2015): 262–275, <https://doi.org/10.1016/j.jfluidstructs.2015.03.004i>.
71. Y. Zhu, Y. Su, and K. Breuer, "Nonlinear Flow-Induced Instability of an Elastically Mounted Pitching Wing," *Journal of Fluid Mechanics* 899 (2020): A35.
72. M. Gharib, E. Rambod, and K. Shariff, "A Universal Time Scale for Vortex Ring Formation," *Journal of Fluid Mechanics* 360 (1998): 121–140, <https://doi.org/10.1017/S0022112097008410>.
73. J. O. Dabiri, "Optimal Vortex Formation as a Unifying Principle in Biological Propulsion," *Annual Review of Fluid Mechanics* 41 (2009): 17–33, <https://doi.org/10.1146/annurev.fluid.010908.165232>.
74. D. Lentink and M. H. Dickinson, "Rotational Accelerations Stabilize Leading Edge Vortices on Revolving Fly Wings," *Journal of Experimental Biology* 212, no. 16 (2009): 2705–2719, <https://doi.org/10.1242/jeb.022269>.
75. B. Liu, A. M. Hamed, Y. Jin, and L. P. Chamorro, "Influence of Vortical Structure Impingement on the Oscillation and Rotation of Flat Plates," *Journal of Fluids and Structures* 70 (2017): 417–427.
76. X. Fan and K. Breuer, "Reduced-Order Modeling of a Bat Flying with Heavy and Highly Articulated Wings," in *AIAA Bio-Inspired Aerodynamics II* (2021), 1–14, <https://doi.org/10.2514/6.2021-0344>.

Supporting Information

Additional supporting information can be found online in the Supporting Information section.

Supporting Figure S1: The flight trajectories at $U = 18 \text{ m/s}$.